JGR Solid Earth

RESEARCH ARTICLE
10.1029/2024JB030075

# Experimental Investigation and Constitutive Description of Mechanical Anisotropy in Soft, Porous Rock

**Julia Leuthold**[1], **Eleni Gerolymatou**[2], **and Theodoros Triantafyllidis**[3]

[1]Department of Civil, Environmental and Geomatic Engineering, ETH Zurich, Zürich, Switzerland, [2]Technical University of Clausthal, Clausthal-Zellerfeld, Germany, [3]Former KIT, Karlsruhe, Germany

**Key Points:**

- The anisotropy of the mechanical behavior of a weak sedimentary rock is experimentally investigated
- Anisotropy results in rotation of the yield loci
- A constitutive description based on the projection method shows good results

**Correspondence to:**
J. Leuthold,
julia.leuthold@igt.baug.ethz.ch

**Citation:**
Leuthold, J., Gerolymatou, E., & Triantafyllidis, T. (2025). Experimental investigation and constitutive description of mechanical anisotropy in soft, porous rock. *Journal of Geophysical Research: Solid Earth*, *130*, e2024JB030075. https://doi.org/10.1029/2024JB030075

Received 2 AUG 2024
Accepted 3 MAY 2025

Correction added on 1 SEP 2025, after first online publication: CSAL funding statement has been added.

**Author Contributions:**
**Funding acquisition:** Theodoros Triantafyllidis
**Investigation:** Julia Leuthold
**Methodology:** Julia Leuthold
**Supervision:** Eleni Gerolymatou, Theodoros Triantafyllidis
**Validation:** Eleni Gerolymatou
**Visualization:** Julia Leuthold
**Writing – original draft:** Julia Leuthold
**Writing – review & editing:** Eleni Gerolymatou, Theodoros Triantafyllidis



**Abstract** The mechanical properties of Maastricht Calcarenite, a carbonatic sandstone with high porosity, are investigated through an extensive laboratory program. The mechanical response under different stress conditions, including compression and extension tests, is studied and the influence of anisotropy is investigated. The test results confirm that the mechanical behavior of the rock is highly anisotropic, resulting in a rotation of the yield loci. The strength and post yield behavior are also affected. The experimental results show that the brittle-ductile transition is independent of the bedding orientation and that the rock fails by the formation of discrete compaction bands in triaxial compression tests at high confining pressures. An analysis of a discrete compaction band on the microscale shows grain crushing. The data obtained in the laboratory is used for the calibration of a simple constitutive model using the projection method, which is then shown to capture anisotropy in the mechanical response.

**Plain Language Summary** This study investigates mechanical properties of Maastricht Calcarenite, a type of sandstone that has a high porosity and behaves like aerated concrete. The researchers conducted a series of tests in the lab for this rock to see how it reacts under different types of stress, like being squeezed and pulled apart. They found that the rock's response to these stresses changes depending on the direction of the rock's layers, a property known as anisotropy. The tests showed that this anisotropy affects both the rock's strength and stiffness. The transition from brittle (where the rock breaks) to ductile (where the rock bends or deforms) doesn't depend on the direction of the rock's layers. When the rock was squeezed under relatively high pressure, it failed by forming distinct bands where it compacted more. Looking closely at these bands, the researchers saw that the grains in the rock were crushed. The data from these tests was then used to create a simple model that can predict how the rock will behave under different stresses, taking into account the anisotropy. This model was successful in capturing the rock's anisotropic behavior.

## 1. Introduction

A significant part of the rocks present in the earth's crust exhibits anisotropy, meaning that it exhibits different physical or mechanical properties when measured along different axes. This characteristic is a result of varying factors, including depositional environments, diagenetic history, and subsequent tectonic deformation and has been observed in most types of rocks, including sedimentary (Oka et al., 2002), metamorphic (Nasseri et al., 2003) and magmatic (Nasseri & Mohanty, 2008; Rawling, 2002) rocks. The implications of the anisotropic nature of rocks and rock mass are fundamental for a large number of applications, such as reservoir engineering, borehole stability (Asaka & Holt, 2021; Ong & Roegiers, 1993), tunneling (Mánica et al., 2023) and nuclear waste disposal (Labiouse et al., 2014). Nonwistanding this, anisotropy is often ignored in applications. The reasons for this are twofold. Firstly, due to the large number of material properties that need to be determined, an extensive testing program is required. This results in significant costs, prohibitive for some applications, and in a large number of specimens being required, posing a difficulty for other applications. Secondly, constitutive modeling of anisotropy is complicated, presents conceptual difficulties and requires the calibration of a large number of parameters.

Previous studies on the anisotropy have shown that a significant number of rocks, especially when foliated, tend to exhibit minimum strength when the cylinder axis and the bedding direction are neither perpendicular nor parallel. In contrast specimens with bedding direction parallel and normal to the cylinder axis exhibit higher, even if not equal, strengths (Crawford et al., 2012; Nasseri & Mohanty, 2008; Rawling, 2002). In triaxial tests on certain sandstones, a minimum has been observed when the bedding direction is parallel to the cylinder axis, rather than

at an inclined angle (Yu et al., 2020). In Brazilian tests a minimum is observed when loaded parallel to the bedding direction (Debecker & Vervoort, 2009).

In most cases the influence of the structural anisotropy on the mechanical behavior of rock is investigated by means of triaxial and isotropic compression tests (Crawford et al., 2012; Crisci et al., 2024; Gatelier et al., 2002; Nasseri & Mohanty, 2008; Niandou et al., 1997; Rawling, 2002). At the same time there is a lack of investigations on the influence of the bedding orientation on the mechanical behavior of rocks under triaxial extensional conditions.

The constitutive description of the anisotropic mechanical response of rock presents some difficulty when compared to its isotropic counterpart. Three general approaches are common. The first is the consideration of anisotropy directly in the formulation of the constitutive equations, in the case of elastoplastic models for example, in the formulation of the yield surface (Hill, 1998; Nova, 1980; Pariseau, 1968). A further common approach is the so called weakness plane category of models, where one failure criterion is used for the rock matrix and another one for the bedding planes (Chen et al., 2008; Lee & Pietruszczak, 2008). The third category of models is based on representation theorems and uses a projection of the stress state to an equivalent stress state where the material can be considered isotropic (Boehler & Sawczuk, 1977; Fu et al., 2012; Semnani et al., 2016).

In the present study the material tested is Tuffeau de Maastricht, a highly porous weak carbonatic rock, which has been previously investigated in other works. Baxevanis et al. (2006) observed the formation of compaction bands under triaxial conditions, accompagnied by a marked reduction in permeability, significantly stronger than would be expected by the Cozeny-Karman law (Carman, 1997; Kozeny, 1927). Leuthold, Gerolymatou, Vergara, and Triantafyllidis (2021) observed a similar permeability reduction and further determined the yield surface, brittle-ductile transition locus and localization behavior based on triaxial tests on specimens cored normal to the bedding axis. These results were simulated in Leuthold, Gerolymatou, and Triantafyllidis (2021), including the localization of deformation using a nonlocal model (Bažant & Pijaudier-Cabot, 1988). Tomography was performed during testing to observe the propagation of compaction bands (Wu et al., 2020). As far as the anisotropy is concerned, experimental results on the same rock showed that the anisotropic structure has a great influence on the mechanical properties (Papazoglou, 2018). A triaxial compression strength decrease of nearly 50% was measured on specimens cored parallel to the bedding planes (P-specimens), compared to the results from specimens cored normal to the bedding planes (S-specimens). However, the experimental investigation was limited to triaxial compression tests.

The present experimental study attempts to fill this void and includes unconfined compressive strength tests, triaxial compression tests, triaxial extension tests, and isotropic compression tests in different orientations with respect to bedding. For completeness, test results from compression tests on specimens cored normal to the bedding planes (S-specimens), already presented in Leuthold, Gerolymatou, Vergara, and Triantafyllidis (2021) are included alongside tests on specimens cored parallel to the bedding planes (P-specimens). Additional individual tests were performed with the cylinder axis at an angle with respect to bedding (Z-specimens). The methods used are outlined in the next section. In the third section results are presented and discussed. The subsequent section is devoted to constitutive modeling and finally conclusions are drawn.

## 2. Experimental Investigation

### 2.1. Material

Calcarenite Tuffeau de Maastricht is a yellowish limestone with a high porosity and a weak cementation between the grains. The rock material is from a quarry next to the city Maastricht in the Netherlands. The mineralogical composition is 98% calcite, the porosity is 50% and the grain density $\rho_s$ is 2.71 g/cm$^3$. Large blocks of the material, 2 m × 1 m × 0.5 m, were obtained with a saw in the quarry itself and brought to the laboratory. The rock looks homogeneous and the bedding planes are not visible with the human eye. At some locations individual shell fragments can be detected and their orientation can be used to determine the orientation of the bedding plane in the rock. The rock consists of shell fragments and bioclasts and, thus, has an intergranular porosity. From a thin section a mean grain size of 100 μm was measured.

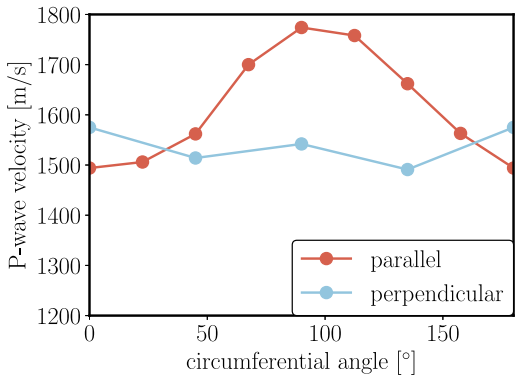


**Figure 1.** P-wave velocity measured in circumferential direction on a P-specimen (parallel) and a S-specimen (perpendicular).

For an initial assessment of the anisotropy, the P-wave velocity of the rock at the circumference of a P-specimen and an S-specimen was measured. Figure 1 shows the measured values for the P-wave velocity plotted versus the circumferential angle.

The P-wave velocities of the S-specimen are almost constant in the circumferential direction, but for the P-specimen a peak at 90° is visible. This confirms that the dynamic elastic properties of the rock are transversely isotropic. Because S-wave velocities were not measured, it is not possible to calculate the dynamic elastic modulus and Poisson's ratio.

### 2.2. Experimental Equipment and Methods

All tests were performed with a test system device model 815 by the company MTS. A more precise description of the test set-up is given in Leuthold, Gerolymatou, Vergara, and Triantafyllidis (2021). 17 of the specimens were S-specimens, 21 P-specimens and four Z-specimens. These were cut with an angle of 30 and 60° between the cylinder axis and the bedding direction. The specimens have a diameter of 70 mm and a length between 140 and 145 mm. The preparation of the specimen and the installation procedure is described in more detail in Leuthold, Gerolymatou, Vergara, and Triantafyllidis (2021).

The experimental program includes unconfined compressive strength tests, triaxial compression tests, triaxial extension tests with decreasing axial stress and increasing confining stress and hydrostatic compression tests. All tests were performed under dry conditions. Unconfined compressive strength tests, triaxial compression tests and strain controlled hydrostatic compression tests were performed with an axial strain rate of 0.01 mm/min. Triaxial extension tests with decreasing axial stress are performed with an axial strain rate of −0.01 mm/min and triaxial extension tests with increasing confining stress are performed with a confining stress rate of 0.1 MPa/min. Triaxial and unconfined compression tests were performed with a spherical seat, triaxial extension tests without. Stress controlled hydrostatic compression tests are performed with a stress rate of 0.90 MPa/min.

### 2.3. Triaxial Compression Tests

Test results of unconfined compressive strength tests and triaxial tests with different confining pressures are shown in Figure 2. Figures 2a and 2c show results of tests on S-specimens and Figures 2b and 2d show results of P-specimens. They indicate that the failure behavior is independent of the bedding orientation as the brittle ductile transition is for both orientations at a confining pressure between 1.0 and 1.5 MPa.

The strength, however, exhibits anisotropy. P-specimens display lower peak strength values. The influence of the bedding orientation is also evident in the post yielding behavior. For S-specimens, stress drops of up to 1 MPa occur at high confining pressures stress. In contrast, for P-specimens, these spontaneous unloadings are less pronounced. Additionally, it is documented that the onset of the hardening behavior occurs at smaller axial strain values for P-specimens compared to S-specimens. This observation suggests that the compaction process varies with the bedding orientation.

Figure 3a shows the failure patterns of S-specimens and Figure 3b shows P-specimens. Steep angle shear bands are documented for low confining pressure levels, whereas discrete compaction bands form during tests at high confining pressures. This observation is independent of the bedding orientation.

The failure pattern observed in the specimen tested at a confining stress of 2.5 MPa indicates that the compaction process initiates at the upper end of the specimen and, with increasing axial strain, propagates to the opposite side. This is similar to what was documented by Klein et al. (2001) for Bentheim sandstone and Olsson (1999) for Castelgate sandstone.

In order to investigate the plastic deformation behavior, the results of the local strain measurement are analyzed. Figure 4 shows the local circumferential strain in the middle of the sample as a function of global axial strain.

As previously discussed, specimens tested at low confining pressures fail through the formation of shear bands. Consequently, the circumference increases during the whole test, as the two forming rock blocks slided past each other. At high confining pressures the circumference remains constant in the midsection of the sample at the onset

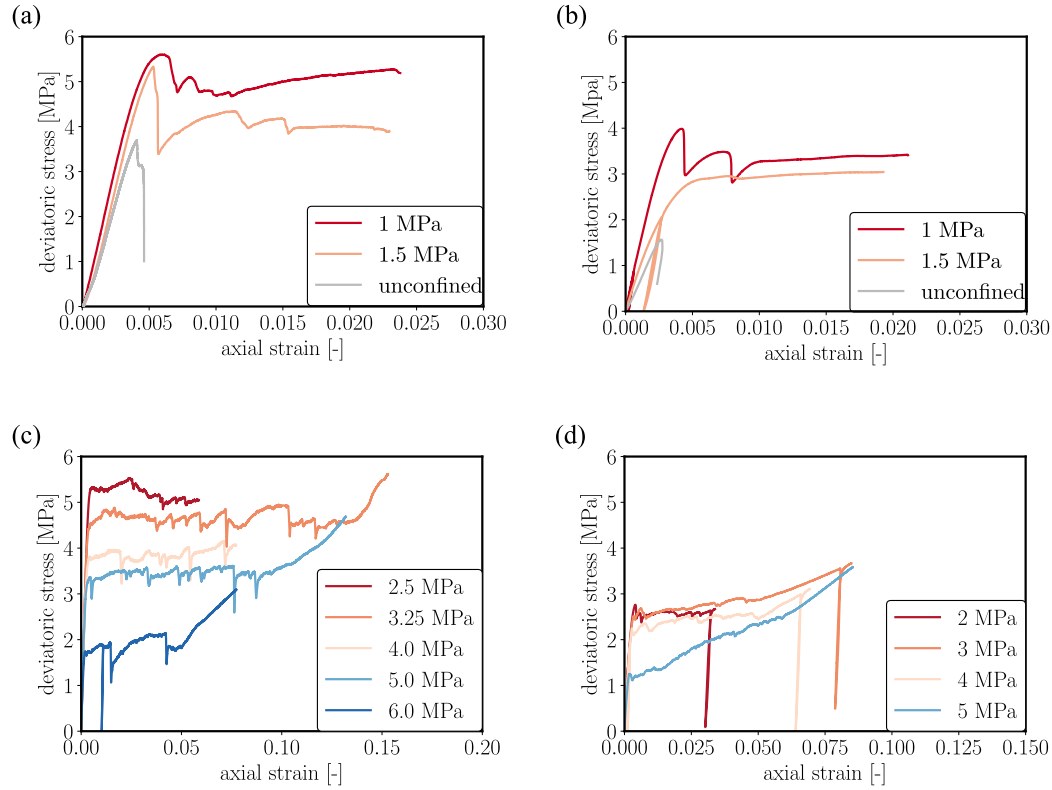


**Figure 2.** Results from unconfined compressive strength and triaxial compression tests, the deviatoric stress is plotted versus axial strain and the value in the legend corresponds to the confining pressure: (a) For S-specimens and (b) P-specimens: unconfined compressive strength and triaxial compression tests at small confining pressures. For S-specimens (c) and P-specimens: (d) Triaxial compression tests at high confining pressures.

of plastic deformation, indicating that the compaction process initiates at the sample ends, as shown in Figure 3 and in other studies in the literature (Holcomb & Olsson, 2003; Papazoglou, 2018). With increasing axial strain the compaction front propagates to the middle of the sample and as soon as it reaches the measurement range of the extensometer the circumferential strain increases or decreases again. This means that the local strain measurement can be used to investigate the compaction process.

The comparison of the results of S-specimens and P-specimens indicate that the compaction process is anisotropic. For P-specimens the circumferential strain is only negative, meaning the circumference increases, whereas for S-specimens the circumference decreases. This could be a result of the smaller strength measured in triaxial tests with P-specimens. Additionally smaller values for the axial strain at the onset of the compaction process in the middle of the sample indicate that less deformation is needed for the compaction parallel than perpendicular to the bedding.

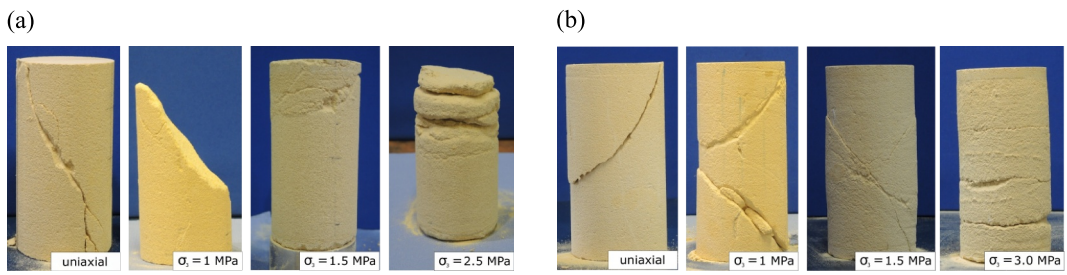


**Figure 3.** Specimens after triaxial compression tests with different confining stress: S-specimens (a) and P-specimens (b).

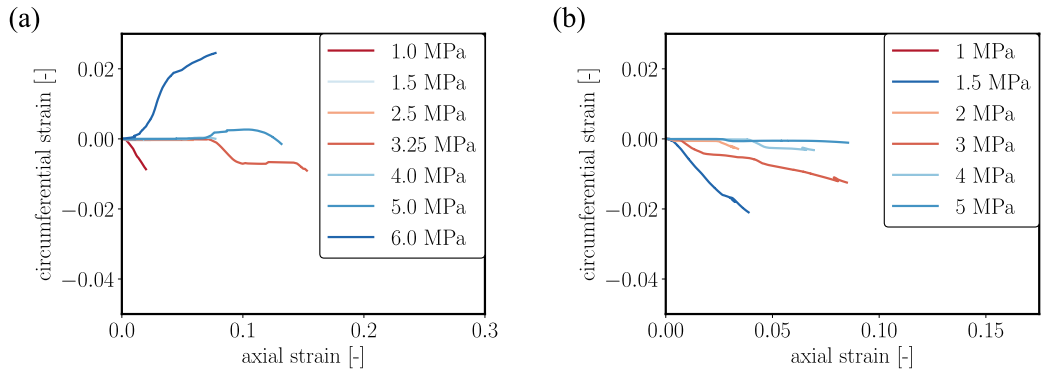


**Figure 4.** Results from triaxial compression tests with different confining pressures, circumferential strain is plotted versus axial strain and the value in the legend corresponds to the confining pressure: S-specimens (a) and P-specimens (b).

Local axial strain was only measured for some tests, because the extensometers used for the local axial measurement should not be deformed beyond 8%. Figure 5 shows the local axial strain as a function of the global axial strain.

Like the results of the circumferential strain measurement, the curve progression for the samples at 2.5 MPa and 4 MPa indicate the evolution of the compaction process. The value for the axial strain at the onset of the compaction process in the measurement range is for P-specimens smaller than for S-specimens. Figure 6 shows the results of unconfined compressive strength tests and triaxial compression tests at a confining pressure of 4 MPa with S-specimens, P-specimens and Z-specimens. While it is known that triaxial loading of Z-specimens leads to the generation of bending moments and can have an effect on the measured strength, this effect was reduced here by the use of a spherical seat. However, a small effect on the experimental results cannot be excluded. In the triaxial tests the circumferential strain was measured and is plotted versus global axial strain.

The results of the unconfined compressive strength tests and the triaxial tests show that the yield strength gradually increases at increasing angle between the load axis and the bedding plane. The evolution of the circumferential strain indicates that the compaction behavior is also affected by the orientation of the bedding plane as the onset of the circumferential strain decrease is at different values for the axial strain. The effect of the anisotropy is not visible in the failure patterns of the samples tested at a confining pressure of 4 MPa, shown in Figure 7.

### 2.4. Triaxial Extension Tests

Triaxial extension tests were performed under different stress conditions. Figure 8 shows the test results of all triaxial extension tests with decreasing axial stress and increasing confining stress. The specimens fail in a brittle manner in extension tests with decreasing axial stress and in a more ductile manner in the tests with increasing

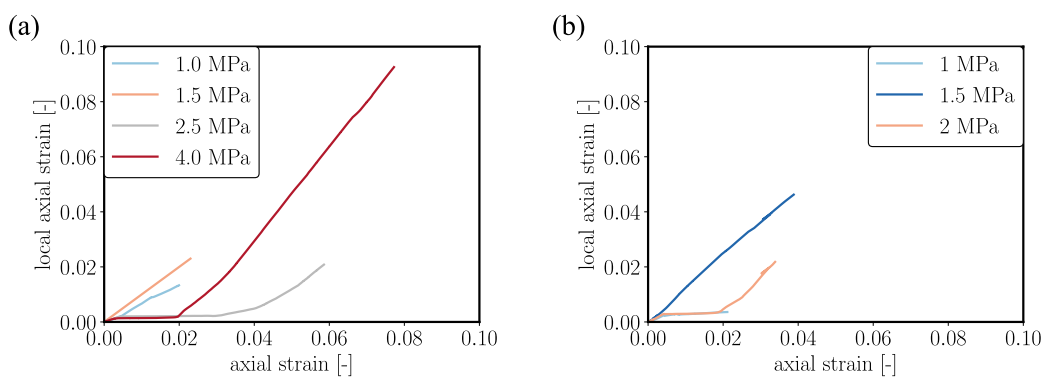


**Figure 5.** Results from triaxial compression tests with different confining pressures, local axial strain is plotted versus global axial strain and the value in the legend corresponds to the confining pressure: S-specimens (a) and P-specimens (b).

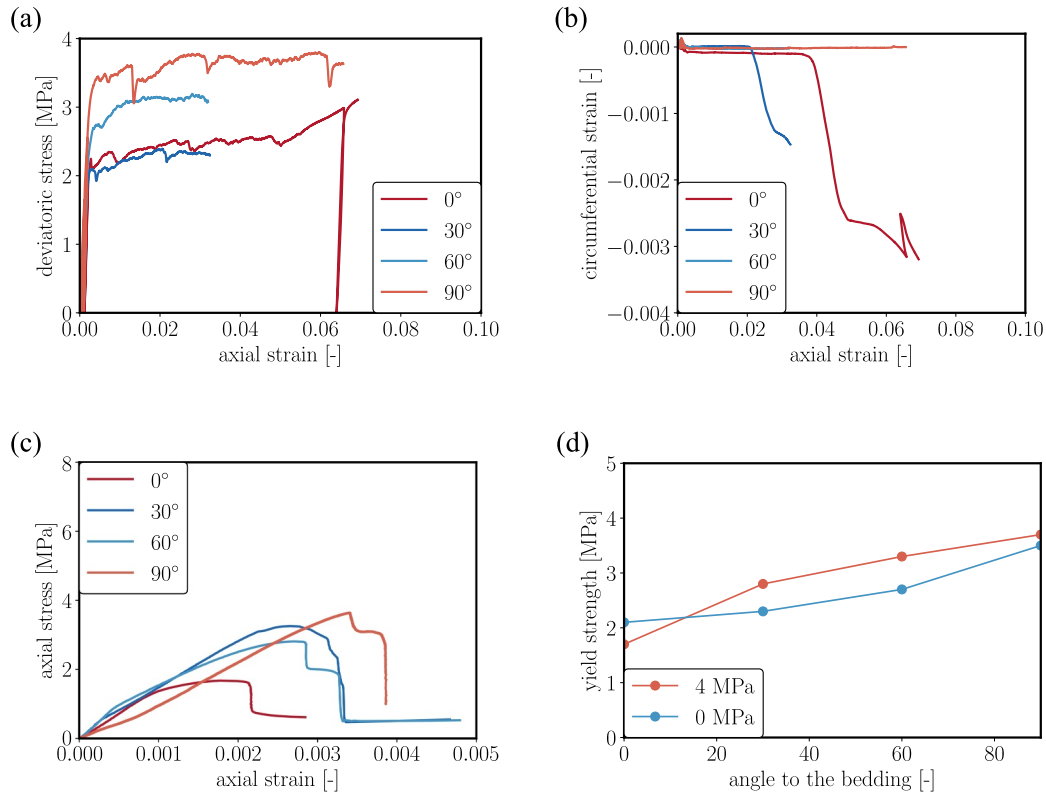


**Figure 6.** Compression tests on specimens with different angles between the cylinder axis and the bedding direction. Triaxial compression tests at a confining pressure of 4 MPa: (a) Deviatoric stress plotted versus global axial strain and (b) circumferential strain plotted versus global axial strain. Unconfined compressive strength test: (c) Axial stress plotted versus global axial strain. Yield strength plotted versus angle between the cylinder axis and the bedding direction (d).

confining pressure. Compared to the results of triaxial compression tests, the effect of the bedding orientation on the strength is smaller. However, it can be noted that the peak strength is slightly higher for P-specimens.

The failure patterns of all specimens after extension with decreasing axial stress are shown in Figure 9.

Intersecting shear bands are clearly visible in most S-specimens and in two P-specimens. The appearance of intersecting rather than single shear bands here is most likely due to the absence of a spherical seat, which was used in the compression tests. Different failure modes located in the middle of the specimen are documented in P-specimens tested at confining pressures smaller than 4 MPa. This can be explained by the fact that the specimens did not fail by the time the axial stress was zero, meaning further axial displacement caused intrusion of the membrane between specimen and loading plate and tearing. For P-specimens tested at a confining pressure of 5 MPa, no defects were detected. Figure 10 shows pictures of the specimens after extension tests with increasing confining pressure.

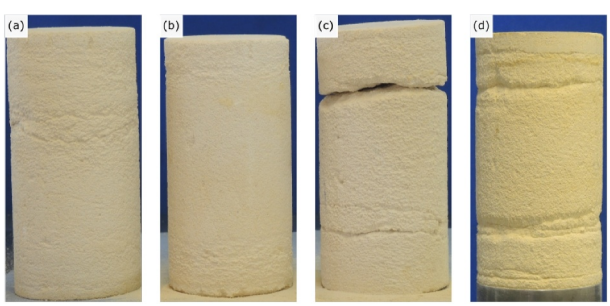


**Figure 7.** S-specimens, P-specimens and Z-specimens (the specified angle is the one between the load axis and the bedding) after triaxial tests at a confining pressure of 4 MPa: (a) Z-specimen (30°), (b) Z-specimen (60°), (c) P-specimen and (d) S-specimen.

Almost all specimens are completely compacted and no defect or deformation band can be detected. Only in a S-specimen tested at an axial stress of 2 MPa and in a P-specimen tested at an axial stress of 4 MPa discrete compaction bands are documented. The compaction band in the S-specimen tested at an axial stress of 2 MPa is not oriented, whereas the compaction band in the P-specimen tested at 4 MPa runs vertically. The vertical orientation of the compaction band in the specimen indicates an effect of the bedding orientation on the formation of compaction bands. It is possible that the documented strain-drop in the deviatoric stress-axial strain curve of the test is an indicator for the formation of the compaction band. A thin section was

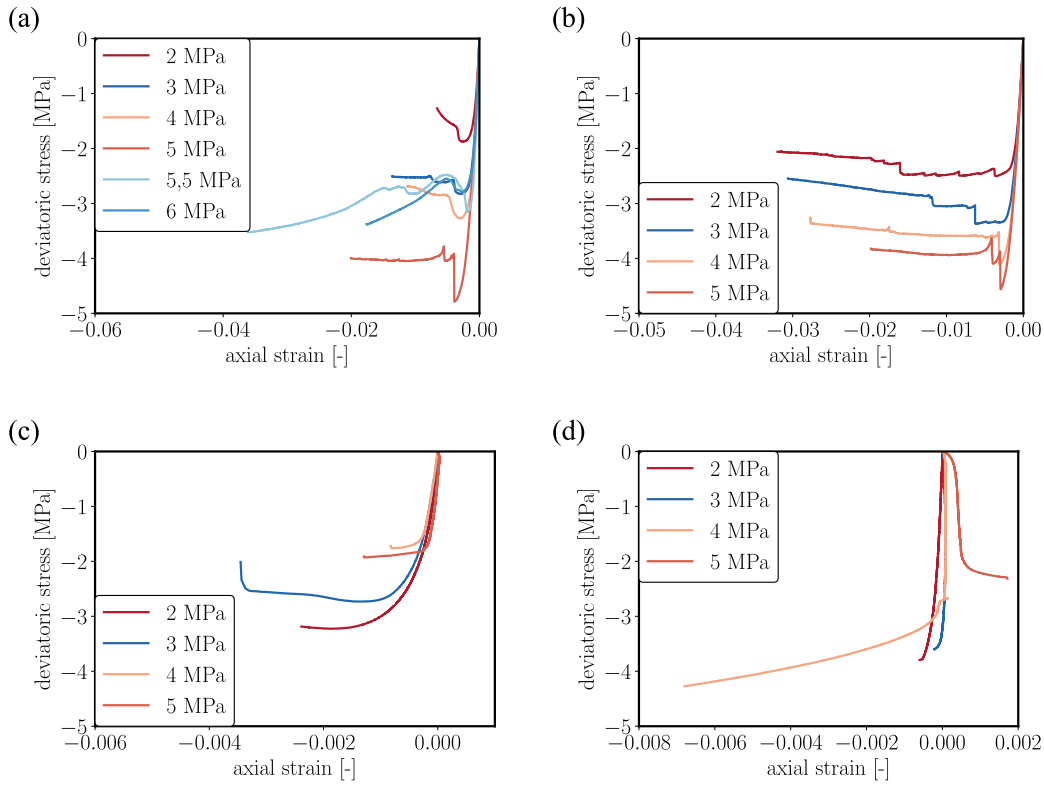


**Figure 8.** Results from triaxial extension tests: For S-specimens (a) and P-specimens (b): Test results form tests with decreasing axial stress at different confining pressures and the value in the legend corresponds to the confining pressure. For S-specimens (c) and P-specimens (d): Test results from tests with increasing confining pressure at different axial stresses and the value in the legend corresponds to the axial stress.

produced from the compaction band and the results are discussed in the section refering to the microstructural analysis. In the P-specimen tested with an axial stress of 2 MPa a different failure pattern than the other specimens can be seen. The reason for the different shape of the specimen is that during the unloading of the specimen the axial piston moved too far down and the specimen was drawn in length.

### 2.5. Hydrostatic Compression Tests

Hydrostatic compression tests were performed with strain control and stress control. Figure 11 shows the test results.

It can be noted that the stress value at the onset of plastic deformation is independent of the bedding orientation and the applied test method. However, the behavior after the plastic onset is anisotropic. For P-specimens the stress does not increase directly at the onset of plastic deformation, but the curve forms a plateau, whereas for S-specimens the hardening phase starts directly at the plastic onset.

## 3. Result Interpretation and Discussion

### 3.1. Microstructural Analysis

In a P-specimen tested in a triaxial extension test at an axial stress of 4 MPa a vertical compaction band was documented after the test. For a microstructural analysis of the band a thin section was produced from the middle part of the specimen. Figure 12 shows pictures of the thin section with different magnifications.

The measured width of the band is around 1 mm and the porosity in the compaction band compared to the surrounded rock is reduced. Closer inspection of the thin sections shows individual grains that are broken, but the major process for the compaction process is pore collapse and not grain crushing.

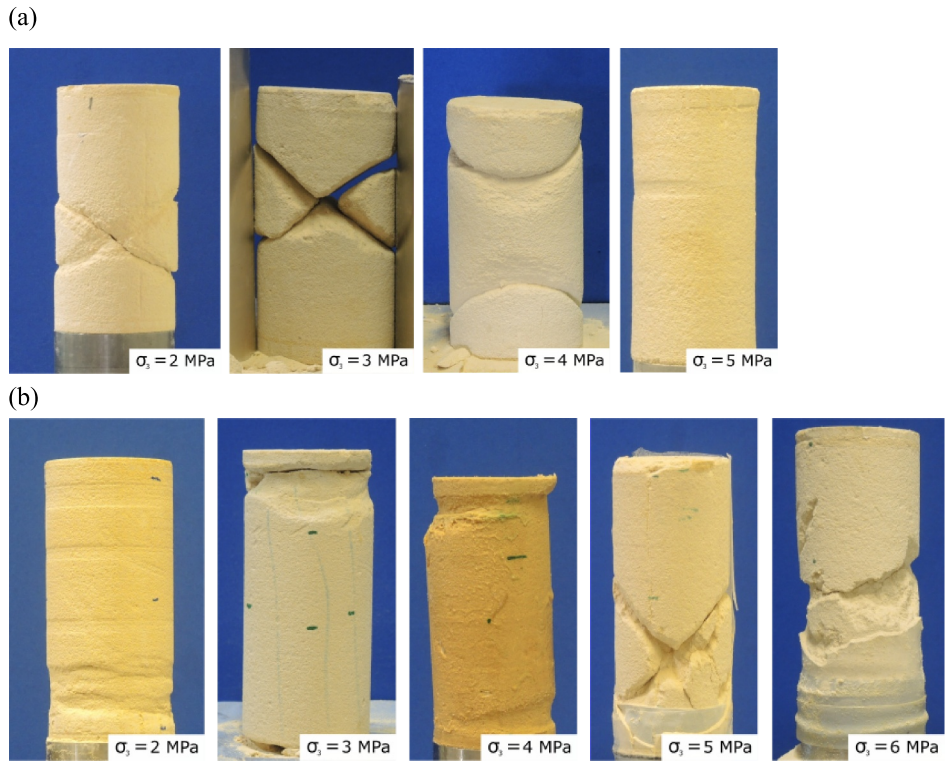


**Figure 9.** Specimens after extension tests with S-specimens (a) and P-specimens (b) at different confining pressures.

### 3.2. Elastic Moduli

For the evaluation of the elastic moduli, unloading and reloading cycles are performed in some triaxial tests. Values for the Young's modulus $E$ and the bulk modulus $K$ are calculated from the results of the strain measurement and shown in Table 1. For the determination of the bulk modulus, the volumetric strain was calculated as a function of global or local axial strain $\epsilon_a$, and the circumferential strain $\epsilon_c$, assuming that the deformation of the cylinder is homogeneous: $\epsilon_v = \epsilon_c + \epsilon_a$.

The results show that the stiffness is higher for S-specimens than for P-specimens though they exhibit significant scatter. This is unusual for most rock types, but has been observed previously in sands (Nishimura & Abdiel, 2017) and calcarenites (Nienhuis & Price, 1990). It is further in agreement with the measured P-wave velocities in the present work.

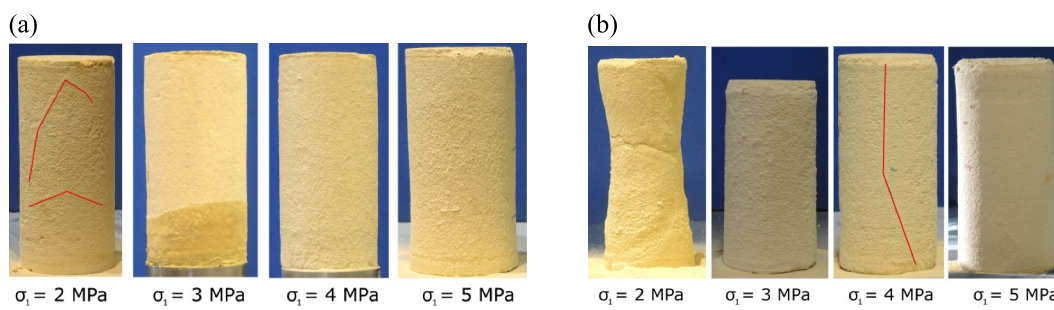


**Figure 10.** Specimens after extension tests with increasing confining stress with S-specimens (a) and P-specimens (b) at different axial stresses.

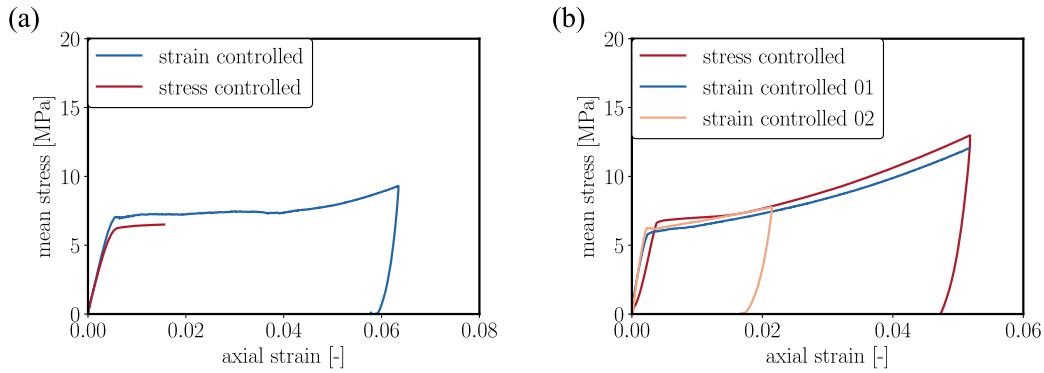


**Figure 11.** Results from hydrostatic compression tests, strain controlled and stress controlled, confining stress is plotted versus global axial strain: (a) P-specimens, (b) S-specimens.

### 3.3. Yield Surface and Flow Directions

The values of the peak strength resulting from all tests with P- and S-specimens are summarized in p-q-diagrams shown in Figure 13. The flow directions determined from the local strain rate measurements are also shown.

In comparison the failure loci look like they are rotated. The failure locus for the S-specimens is rotated upwards and the one from the tests with P-specimens is rotated downwards. Moreover, the elastic domain is larger for the S-specimens than the P-specimens.

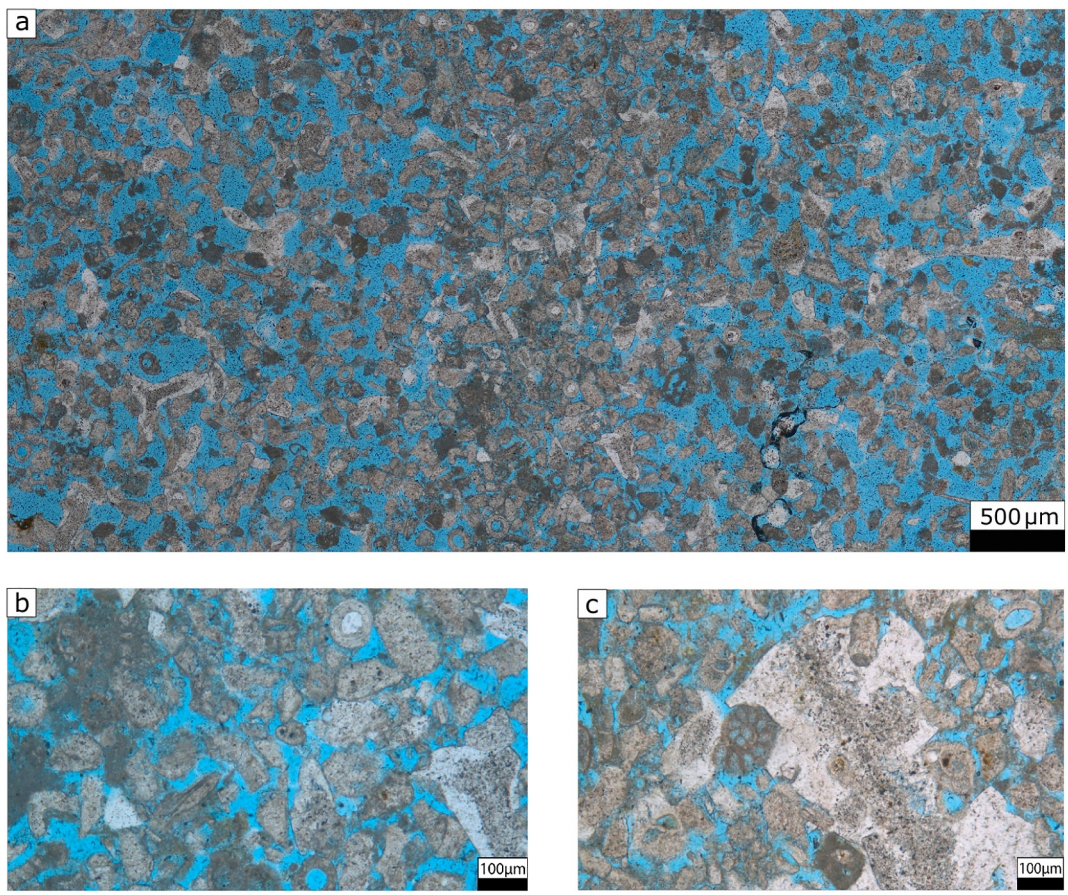


**Figure 12.** A microscopic image of a thin section that is taken from a P-specimen tested in an extension test with an axial stress of 4 MPa, in the middle of picture (a). A compaction band (b) and the thin section (c) is shown in smaller scale.

**Table 1**
*Elastic Moduli From S-Specimens and P-Specimens*

| Test | Specimen Type | $E_{local}$ MPa | $E_{glob}$ MPa | $K_{loc}$ MPa | $K_{glob}$ MPa |
|---|---|---|---|---|---|
| Unconfined | S | 2,730 | 2,240 | – | – |
| Unconfined | P | – | 1,753 | – | – |
| 1.0 MPa | S | – | – | – | – |
| 1.0 MPa | P | 1,585 | 2,312 | – | – |
| 1.5 MPa | S | – | – | – | – |
| 1.5 MPa | P | 1,676 | 1,624 | – | – |
| 2.0 MPa | P | 2,230 | 787 | – | – |
| 2.5 MPa | S | – | – | – | – |
| 3.0 MPa | P | – | – | – | – |
| 3.25 MPa | S | – | 1,160 | – | – |
| 4.0 MPa | S | 3,524 | 2,647 | – | – |
| 4.0 MPa | P | – | 1,578 | – | – |
| 5.0 MPa | S | – | – | – | – |
| 5.0 MPa | P | – | – | – | – |
| 6.0 MPa | S | – | – | – | – |
| Hydro | S | – | – | 700 | 785 |
| Hydro | P | – | – | 1,115 | 815 |

Under the assumption of a homogeneous deformation at failure, the volumetric strain $\epsilon_v$ and the deviatoric strain $\epsilon_q$ can be calculated with the following equations:

$$\dot{\epsilon}_v = 2\dot{\epsilon}_c + \dot{\epsilon}_a \tag{1}$$

$$\dot{\epsilon}_q = \frac{2}{3}\left(\dot{\epsilon}_a - \dot{\epsilon}_c\right). \tag{2}$$

with $\dot{\epsilon}_c$ being the local circumferential strain rate and $\dot{\epsilon_a}$ the global axial strain rate. For the specimens that fail by the formation of shear bands the flow direction is determined after the peak strength. Since the global axial strain is utilized to calculate the axial strain rate, localized deformations are not fully accounted for in the assessment of the flow direction. Figure 14a shows the experimental results of a test with a confining pressure of 1.5 MPa, the deviatoric stress and the deviatoric strain are plotted versus volumetric strain. As the failure behavior is brittle and accompanied by a loss of control after the failure, the deviatoric strain and the volumetric strain increment after the failure are both negative. This is an artifact of the loss of control.

Specimens that fail by the formation of compaction bands are more complex, because here the flow direction is determined at the onset of compaction in the middle of the specimen when the compaction front reaches the measurement range of the circumferential strain extensometer. Figure 14b shows the results from the triaxial test at a confining pressure of 3.25 MPa. The circumferential strain and the deviatoric strain are plotted versus volumetric strain. Volumetric strain increases during the whole test. The flow direction is determined when the circumferential strain begins to change, because this marks the onset of the compaction process.

The flow directions determined in this way are shown in Figure 13. The direction of the flow rates that results from the tests fulfill the thermodynamic conditions, except for the triaxial compression test at a confining pressure of 1.5 MPa that was shown before. The flow directions of all hydrostatic tests are not horizontal, but with a positive or negative inclination. That leads to the conclusion that the yield loci are rotated, assuming an associated flow rule. Moreover, the flow directions of all tests are closer to an associative flow rule than expected. However, the results reveal the effect of the bedding orientation on the yield locus.

## 4. Constitutive Approach

To simulate the experimental results a constitutive model outlined in Leuthold, Gerolymatou, and Triantafyllidis (2021) was used and extended to account for the anisotropic strength of the rock.

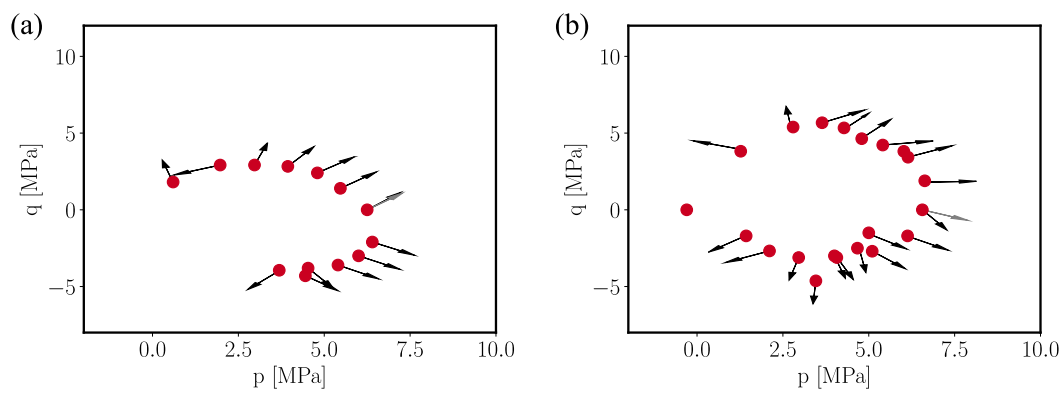


**Figure 13.** The yield surface and the flow direction that results from tests S-specimens (a, b) P-specimens.

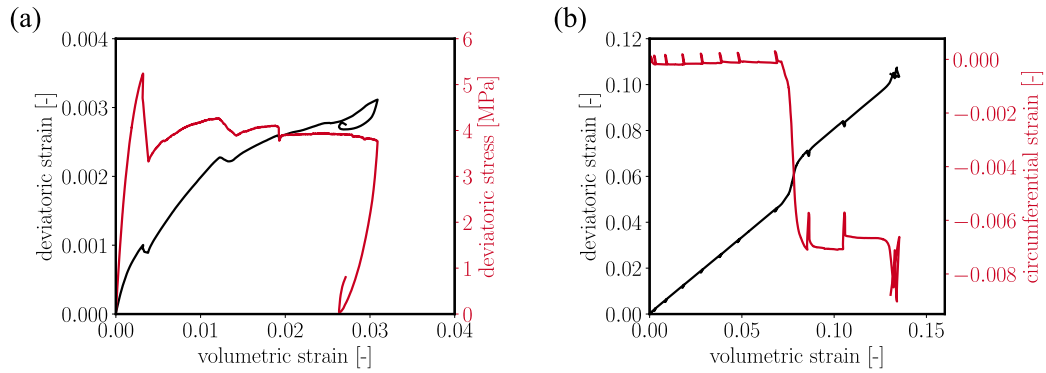


**Figure 14.** Results from the triaxial compression test at a confining pressure of 1.5 MPa (a) and 3.25 MPa (b): In panel (a) deviatoric stress and deviatoric strain are plotted versus volumetric strain (b) circumferential strain and deviatoric strain are plotted versus volumetric strain.

For the formulation of the isotropic yield surface a model by Leuthold, Gerolymatou, Vergara, and Triantafyllidis (2021) is used. The yield function is expressed with the following equation:

$$f = q^2 + M_f h(p)(p - p_t)(p - p_c) \leq 0. \tag{3}$$

Function $h(p)$ has the following form:

$$h(p) = \exp\left[-\frac{1}{\beta}\left(\frac{p - p_t}{p_c - p_t} - \alpha\right)^2\right]. \tag{4}$$

In the expression, $p_t$ is the tensile strength, $p_c$ the strength at isotropic compression and $\alpha$ and $\beta$ are material parameters.

To describe the softening and hardening behavior of the rock a model by Nova et al. (2003) is chosen. In this model it is assumed that:

$$p_c = p_s + p_m, \tag{5}$$

where $p_s$ represents the effect of the strength of the grains and $p_m$ the influence of internal bonding. The evolution of state variables depends on the elasto-plastic strain and as in Nova et al. (2003), it is assumed that

$$\dot{p}_s = \rho_s p_s \left(\dot{\epsilon}_v^p + \xi_s \dot{\epsilon}_q^p\right), \tag{6}$$

where $\rho_s$ and $\xi_s$ are material constants. The following evolution equation is for the state variable $p_m$

$$\dot{p}_m = -\rho_m p_m \left(\left|\dot{\epsilon}_v^p\right| + \xi_m \dot{\epsilon}_q^p\right), \tag{7}$$

with the material parameters $\rho_m$ and $\xi_m$.

To account for the anisotropic strength of the rock the stress projection approach, introduced by Boehler and Sawczuk (1977), was used, resulting in the following projection:

$$\sigma_{ij}^* = \sigma_{ij} + c_1 \cdot M_{ik}\sigma_{kl}M_{lj} + c_2(M_{ik}\sigma_{kj} + \sigma_{ik}M_{kj}) \tag{8}$$

where $M_{ij}$ is an anisotropy tensor, defined as

**Table 2**
*Projection Parameters*

| Parameter | $p_c$ | $p_t$ | $\alpha$ | $\beta$ | $M_f$ | $c_1$ | $c_2$ | $\rho_s$ | $\xi_s$ | $\rho_m$ | $\xi_m$ | $E$ | $\nu$ |
|---|---|---|---|---|---|---|---|---|---|---|---|---|---|
| Unit | MPa | MPa | – | – | – | – | – | – | – | – | – | MPa | – |
| Value | 6.2 | 0.3 | 0.55 | 0.3 | 1.2 | 0.9 | 1.0 | 25 | 0.2 | 0.75 | −1.5 | 2,000 | 0.12 |

$$M_{ij} = e_i \cdot e_j \tag{9}$$

$\sigma^*_{ij}$ being the projected stress tensor and $e_i$ being the unit normal vector defining the axis of symmetry. The calibrated parameter set for the stress projection can be found in Table 2.

Figure 15a shows projected experimental results and the calibrated yield surface. Calibration results show that the projection method is capable to describe a yield surface in the isotropic stress space. A comparison between experimental curves and numerically calculated curves is shown in Figures 15b and 15c. The element test program used for the calculation is based on the Incremental Driver (Niemunis, 2014). While the fit is only adequate due to the simple nature of the model, the anisotropy of the mechanical response is captured well.

## 5. Conclusions

In the present work a series of tests under triaxial conditions were performed on a soft sedimentary rock. Tuffeau de Maastricht sandstone was found to present transverse isotropy based on P-wave velocity measurements, with higher velocities normal to the bedding than parallel to it. The experimental test results are in accordance with this observation. In compression higher strengths are observed in S-specimen, while in extension the differences are minimal. Testing with Z-specimen showed a monotonic variation of the strength with inclination to the bedding.

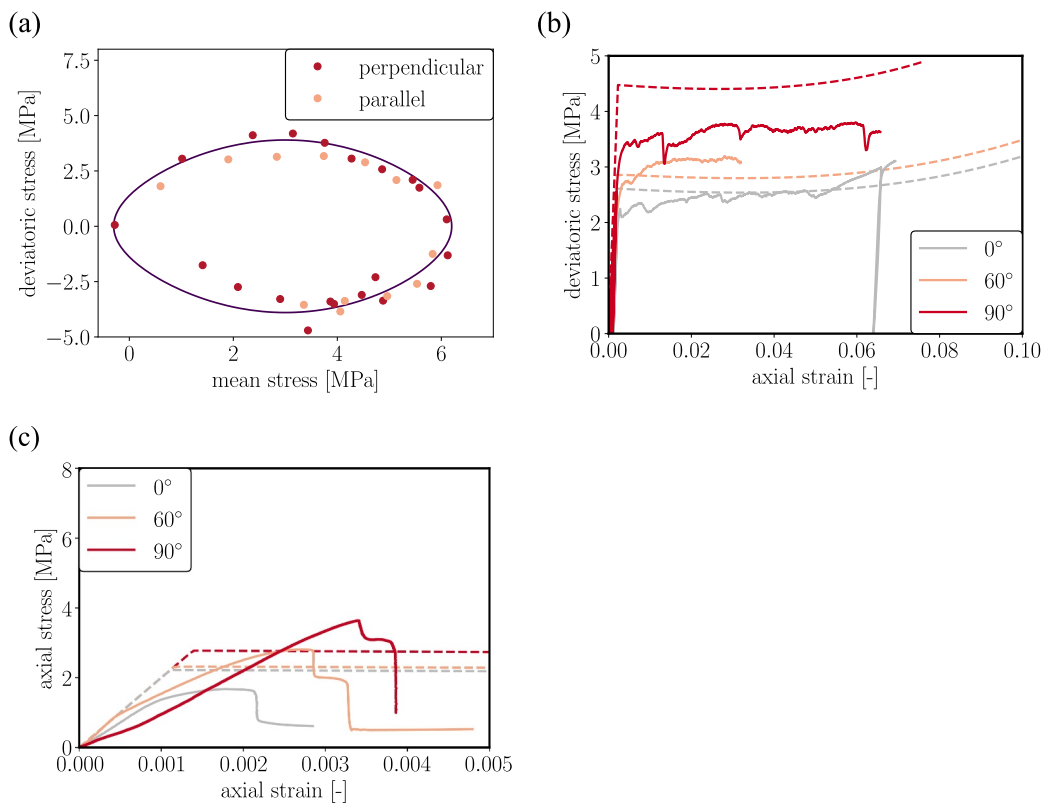


**Figure 15.** Experimental results and results from numerical calculations with one Gauss point, (a) yield surface, (b) confining pressure 4 MPa, (c) unconfined compressive strength tests.

In both directions, the material exhibited the formation of shear bands at low confining stresses and compaction bands at high confining stresses, both in compression and in extension. This indicates that soft sedimentary rocks can behave in a qualitatively different manner to rocks with weakness planes.

The experimental results were simulated using a simple constitutive model based on projection. The results, though acceptable, indicate that accurate simulation requires sophisticated models. This is especially the case in the post yield domain, where the rock exhibits a non-associative response, as evidenced by local strain measurements. From this, it is clear that local strain measurements are important for model calibration, including flow directions, as well as for the determination of the elastic parameters.

## Data Availability Statement

The experimental data supported this study can be found at (Leuthold & Gerolymatou, 2024a). And the subroutine used for the numerical calculations at (Leuthold & Gerolymatou, 2024b).

**Acknowledgments**

The experimental work was conducted as part of Julia Leuthold's PhD thesis during her tenure at the institute for soil and rock mechanics at KIT in Karlsruhe, under the supervision of Prof. Triantafyllidis. The authors extend their sincere gratitude to the reviewers for their constructive feedback and valuable suggestions, which significantly improved the quality of this manuscript. Special thanks are also due to the associate editor and the editor for their insightful guidance and meticulous attention to detail throughout the review process. We are deeply appreciative of the technical staff who provided invaluable assistance in specimen preparation. Their expertise and dedication were critical to the successful completion of this work. A special thanks also goes to Benjamin Busch and Alexander Monsees for their support in the production and analysis of thin sections. Open access publishing facilitated by Eidgenossische Technische Hochschule Zurich, as part of the Wiley - Eidgenossische Technische Hochschule Zurich agreement via the Consortium Of Swiss Academic Libraries.

## References

Asaka, M., & Holt, R. M. (2021). Anisotropic wellbore stability analysis: Impact on failure prediction. *Rock Mechanics and Rock Engineering*, *54*(2), 583–605. https://doi.org/10.1007/s00603-020-02283-0

Baxevanis, T., Papamichos, E., Flornes, O., & Larsen, I. (2006). Compaction bands and induced permeability reduction in Tuffeau de Maastricht calcarenite. *Acta Geotechnica*, *1*(2), 123–135. https://doi.org/10.1007/s11440-006-0011-y

Bažant, Z. P., & Pijaudier-Cabot, G. (1988). Nonlocal continuum damage, localization instability and convergence. *Journal of Applied Mechanics, Transactions ASME*, *55*(2), 287–293. https://doi.org/10.1115/1.3173674

Boehler, J., & Sawczuk, A. (1977). On yielding of oriented solids. *Acta Mechanica*, *27*(1–4), 185–204. https://doi.org/10.1007/bf01180085

Carman, P. G. (1997). Fluid flow through granular beds. *Chemical Engineering Research and Design*, *75*(Supplement), 32–48. https://doi.org/10.1016/s0263-8762(97)80003-2

Chen, X., Yang, Q., Qiu, K., & Feng, J. (2008). An anisotropic strength criterion for jointed rock masses and its application in wellbore stability analyses. *International Journal for Numerical and Analytical Methods in Geomechanics*, *32*(6), 607–631. https://doi.org/10.1002/nag.638

Crawford, B. R., DeDontney, N. L., Alramahi, B., & Ottesen, S. (2012). Shear strength anisotropy in fine-grained rocks. In *46th US rock mechanics/geomechanics symposium 2012* (Vol. 1, pp. 425–436).

Crisci, E., Giger, S., Laloui, L., Ferrari, A., Ewy, R., Stankovic, R., et al. (2024). *Insights from an extensive triaxial testing campaign on a shale for comparative site characterization of a deep geological repository*. (Vol. 38). Geomechanics for Energy and the Environment. https://doi.org/10.1016/j.gete.2023.100508.100508

Debecker, B., & Vervoort, a. (2009). Experimental observation of fracture patterns in layered slate. *International Journal of Fracture*, *159*(1), 51–62. https://doi.org/10.1007/s10704-009-9382-z

Fu, Y., Iwata, M., Ding, W., Zhang, F., & Yashima, A. (2012). An elastoplastic model for soft sedimentary rock considering inherent anisotropy and confining-stress dependency. *Soils and Foundations*, *52*(4), 575–589. https://doi.org/10.1016/j.sandf.2012.07.001

Gatelier, N., Pellet, F., & Loret, B. (2002). Mechanical damage of an anisotropic porous rock in cyclic triaxial tests. *International Journal of Rock Mechanics and Mining Sciences*, *39*(3), 335–354. https://doi.org/10.1016/s1365-1609(02)00029-1

Hill, R. (1998). *The mathematical theory of plasticity* (Vol. 11). Oxford University Press.

Holcomb, D. J., & Olsson, W. A. (2003). Compaction localization and fluid flow. *Journal of Geophysical Research*, *108*(B6), 1–13. https://doi.org/10.1029/2001JB000813

Klein, E., Baud, P., Reuschlé, T., & Wong, T. (2001). Mechanical behaviour and failure mode of Bentheim sandstone under triaxial compression. *Physics and Chemistry of the Earth*, *26*(1–2), 21–25. Retrieved from http://www.sciencedirect.com/science/article/pii/S1464189501000175

Kozeny, J. (1927). Über kapillare Leitung des Wassers im Boden. *Akademie der Wissenschaften Wien*, *136*, 271–306.

Labiouse, V., Sauthier, C., & You, S. (2014). Hollow cylinder simulation experiments of galleries in boom clay formation. *Rock Mechanics and Rock Engineering*, *47*(1), 43–55. https://doi.org/10.1007/s00603-012-0332-0

Lee, Y.-K., & Pietruszczak, S. (2008). Application of critical plane approach to the prediction of strength anisotropy in transversely isotropic rock masses. *International Journal of Rock Mechanics and Mining Sciences*, *45*(4), 513–523. https://doi.org/10.1016/j.ijrmms.2007.07.017

Leuthold, J., & Gerolymatou, E. (2024a). Experimental data from triaxial compression and extension tests on Calcarenite specimens oriented at different angles to the bedding plane [Dataset]. *Zenodo*. https://doi.org/10.5281/zenodo.13164716

Leuthold, J., & Gerolymatou, E. (2024b). User material subroutine for abaqus: Soft, porous, and anisotropic rocks [Software Code]. *GitHub*. https://doi.org/10.5281/zenodo.15118471

Leuthold, J., Gerolymatou, E., & Triantafyllidis, T. (2021). Effect of compaction banding on the hydraulic properties of porous rock - Part II: Constitutive description and numerical simulations. *Rock Mechanics and Rock Engineering*, *54*(6), 2685–2696. https://doi.org/10.1007/s00603-021-02430-1

Leuthold, J., Gerolymatou, E., Vergara, M. R., & Triantafyllidis, T. (2021). Effect of compaction banding on the hydraulic properties of porous rock: Part I—Experimental investigation. *Rock Mechanics and Rock Engineering*, *54*(6), 2671–2683. https://doi.org/10.1007/s00603-021-02427-w

Mánica, M. A., Gens, A., Vaunat, J., Armand, G., & Vu, M.-N. (2023). Anisotropy effects on the response of deep tunnels excavated in claystone. In *Isrm congress* (pp. ISRM–15CONGRESS).

Nasseri, M., & Mohanty, B. (2008). Fracture toughness anisotropy in granitic rocks. *International Journal of Rock Mechanics and Mining Sciences*, *45*(2), 167–193. https://doi.org/10.1016/j.ijrmms.2007.04.005

Nasseri, M., Rao, K., & Ramamurthy, T. (2003). Anisotropic strength and deformation behavior of Himalayan schists. *International Journal of Rock Mechanics and Mining Sciences*, *40*(1), 3–23. https://doi.org/10.1016/S1365-1609(02)00103-X

Niandou, H., Shao, J., Henry, J., & Fourmaintraux, D. (1997). Laboratory investigation of the mechanical behaviour of tournemire shale. *International Journal of Rock Mechanics and Mining Sciences*, *34*(1), 3–16. https://doi.org/10.1016/s0148-9062(96)00053-8

Niemunis, A. (2014). Incremental driver. Retrieved from https://soilmodels.com/idriver/

Nienhuis, H., & Price, D. G. (1990). The scale effect with regard to the deformability of calcarenite. *Geological Society, London, Engineering Geology Special Publications*, *6*(1), 205–215. https://doi.org/10.1144/GSL.ENG.1990.006.01.23

Nishimura, S., & Abdiel, M. D. (2017). Cataloguing stiffness anisotropy of natural sedimentary soils – From clays to intermediate soils. *Japanese Geotechnical Society Special Publication*, *5*(2), 101–106. https://doi.org/10.3208/jgssp.v05.021

Nova, R. (1980). The failure of transversely isotropic rocks in triaxial compression. *International Journal of Rock Mechanics and Mining Sciences*, *17*(6), 325–332. https://doi.org/10.1016/0148-9062(80)90515-X

Nova, R., Castellanza, R., & Tamagnini, C. (2003). A constitutive model for bonded geomaterials subject to mechanical and/or chemical degradation. *International Journal for Numerical and Analytical Methods in Geomechanics*, *27*(9), 705–732. https://doi.org/10.1002/nag.294

Oka, F., Kimoto, S., Kobayashi, H., & Adachi, T. (2002). Anisotropic behavior of soft sedimentary rock and a constitutive model. *Soils and Foundations*, *42*(5), 59–70. https://doi.org/10.3208/sandf.42.5_59

Olsson, W. (1999). Theoretical and experimental investigation of compaction bands in porous rock. *Journal of Geophysical Research*, *104*(B4), 7219–7228. https://doi.org/10.1029/1998jb900120

Ong, S., & Roegiers, J.-C. (1993). Influence of anisotropies in borehole stability. *International Journal of Rock Mechanics and Mining Sciences and Geomechanics Abstracts*, *30*(7), 1069–1075. https://doi.org/10.1016/0148-9062(93)90073-M

Papazoglou, A. (2018). *An experimental study of localized compaction in high porosity rocks: the example of tuffeau de maastricht (Unpublished doctoral dissertation)*. Université Grenoble Alpes.

Pariseau, W. (1968). Plasticity theory for anisotropic rocks and soil. In *The 10th u.s. symposium on rock mechanics (usrms)* (pp. 267–295).

Rawling, G. C., Baud, P., & Wong, T. (2002). Dilatancy, brittle strength, and anisotropy of foliated rocks: Experimental deformation and micromechanical modeling. *Journal of Geophysical Research*, *107*(B10), 2234. https://doi.org/10.1029/2001JB000472

Semnani, S., White, J., & Borja, R. (2016). Thermoplasticity and strain localization in transversely isotropic materials based on anisotropic critical state plasticity. *International Journal for Numerical and Analytical Methods in Geomechanics*, *40*(18), 2423–2449. https://doi.org/10.1002/nag.2536

Wu, H., Papazoglou, A., Viggiani, G., Dano, C., & Zhao, J. (2020). Compaction bands in Tuffeau de Maastricht: Insights from X-ray tomography and multiscale modeling. *Acta Geotechnica*, *15*(1), 39–55. https://doi.org/10.1007/s11440-019-00904-9

Yu, J., Yao, W., Duan, K., Liu, X., & Zhu, Y. (2020). Experimental study and discrete element method modeling of compression and permeability behaviors of weakly anisotropic sandstones. *International Journal of Rock Mechanics and Mining Sciences*, *134*(May), 104437. https://doi.org/10.1016/j.ijrmms.2020.104437